Photocatalytic selective oxidation of methane by quantum sized bismuth vanadate

Yingying Fan (ccyyfan@gzhu.edu.cn)
Guangzhou University
Wencai Zhou
National Center for Nanoscience and Technology
Xueying Qiu
National Center for Nanoscience and Technology
Hongdong Li
National Center for Nanoscience and Technology
Yuheng Jiang
National Center for Nanoscience and Technology
Zhonghui Sun
Guangzhou University
Dongxue Han
Guangzhou University
Li Niu
Guangzhou University
Zhiyong Tang
National Center for Nanoscience and Technology https://orcid.org/0000-0003-0610-0064

Article

Keywords: C1 Oxygenates, Nanoparticles, Radical Reaction Mechanism

Posted Date: October 13th, 2020

DOI: https://doi.org/10.21203/rs.3.rs-86287/v1

Version of Record: A version of this preprint was published at Nature Sustainability on February 4th, 2021. See the published version at https://doi.org/10.1038/s41893-021-00682-x.

Abstract

Selective oxidation of methane to desirable C1 oxygenates has long been the major challenge in catalysis. Here we report photocatalytic oxidation of methane by using quantum-sized bismuth vanadate nanoparticles as catalyst and oxygen as mild oxidant. A high selectivity towards methanol (1.1 mmol g-1 yield and 96.6% selectivity) and formaldehyde (13.1 mmol g-1 yield and 86.7% selectivity) products is successfully realized by simply controlling the light wavelength, light energy, reaction time and the amount of water solvent. Comprehensive characterizations disclose that the radical reaction mechanism is responsible for this efficient photocatalytic methane conversion.

Introduction

Methane (CH_4), approximately occupying 70% to 90% in natural gas[1, 2], has been broadly recognized as an indispensable feedstock in the manufactures of fuels and chemicals with high added-values[3, 4]. Traditional industrial technology has succeeded in implementing large-scale transformation of CH_4 to liquid chemicals via an indirect mode, involving the first syngas (H_2 and CO) formation and the second downstream process[5, 6]. Obviously, the divided reaction steps and required high operation temperature (800 - 900^oC)[7] are the formidable challenges for modern sustainable development.

Taking light illumination instead of high-temperature heating, photocatalytic CH_4 oxidation holds the great promise to transform CH_4 into many types of high valued liquid chemicals at room temperature[8, 9]. Amongst the investigated liquid products, methanol (CH_3OH) and formaldehyde (HCHO) are two major targets because of their roles as the basic and widely used chemicals[10, 11, 12]. Until now, a few photocatalytic CH_4 conversions with satisfied yield of CH_3OH and HCHO have been reported; for instance, photocatalytic oxidation of CH_4 over 0.1 wt% Au/ZnO and 0.1 wt% Ag/ZnO achieved 41.2 μmol CH_3OH (15.7% selectivity) and 112.1 μmol HCHO (42.6% selectivity)[12], respectively, under moderate reaction condition.

Noteworthily, there has been always a serious dilemma between the productivity and selectivity for CH_4 oxidation, which is a complicated and energy-downhill process of $CH_4 \rightarrow CH_3OOH \rightarrow CH_3OH \rightarrow HCHO \rightarrow CO_2$[13, 14, 15, 16, 17] (Fig. 1), and the undesired intermediates and overoxidation always exist. To be specific to the formation of CH_3OH, optimizing its selectivity needs maximizing the reduction of CH_3OOH while preventing the overoxidation to HCHO and CO_2. Similarly, to promote the selectivity of HCHO, CH_3OH intermediates must be further oxidized whilst avoiding overoxidation to CO_2.

Herein, we suggest a highly selective aerobic conversion of CH_4 to CH_3OH and HCHO at room temperature using quantum-sized $BiVO_4$ nanoparticles (q-$BiVO_4$) as photocatalyst. On the basis of the maximum yield (1.1 mmol g^{-1} CH_3OH or 13.1 mmol g^{-1} HCHO), the selectivity of CH_3OH and HCHO

reaches 96.6% and 86.7%, respectively. The q-$BiVO_4$ is characteristic of high kinetic energy of charge carrier and large specific surface, enabling effective conversion of CH_4 into CH_3OH and HCHO. By altering the amount of oxygen (O_2) and solvent (H_2O), reaction time, irradiation wavelength and light intensity, the selectivity towards CH_3OH and HCHO is rationally tuned. The aerobic oxidation of CH_4 is disclosed to be proceeded with a radical mechanism according to the isotopic test ($^{13}CH_4$, $H_2{}^{18}O$, $^{18}O_2$ and CD_4), intermediate capture and rate-determining step determination.

Results

Preparation and characterizations of $BiVO_4$ photocatalysts. We hypothesize that the low photocatalytic activity of commonly-used submicro-sized $BiVO_4$ particles (s-$BiVO_4$) originates from their rather narrow bandgap and small surface-to-volume ratio. Therefore, a hard-template method was developed for preparing q-$BiVO_4$ with shrunk size, which would have an increased bandgap and larger surface-to-volume ratio. As shown in Fig. 2a, homogeneous blending of silica gels with $Bi(NO_3)_3$ and NH_4ViO_3 precursors followed by calcination resulted in a composite structure with silica template encapsulated by $BiVO_4$ (Fig. S1). Subsequent high-pressure hydrothermal reaction made silica template fully dissolve, which broke $BiVO_4$ shell into quantum sized particles. Transmission electron microscopy (TEM) images reveal that the spherical aggregates (Fig. 2b, c) are composed of point-like q-$BiVO_4$ with an average particle size of ~ 4.5 nm (Fig. 2d, e). It is known that the Bohr radius of $BiVO_4$ is about 2 nm[18, 19] which is close to the radius of q-$BiVO_4$ (2.25 nm). Thus, q-$BiVO_4$ should exhibit a strong quantum confinement effect. X-ray diffraction (XRD) pattern indicates that as-synthesized q-$BiVO_4$ is of monoclinic scheelite structure without any impurity crystal phase (Fig. 2g and Fig. S2). Note that the absence of broad XRD shoulder corresponding to amorphous silica manifests the successful removal of template (Fig. S2). The characteristic XRD peaks are also used to analyze the average aggregation size of q-$BiVO_4$ (10.5 nm) within Debye-Scherrer method (Fig. S3). The clear lattice fringe in high-resolution TEM (HRTEM, Fig. 2f) and the selected area electron diffraction (SAED) pattern both confirm the high crystalline nature of q-$BiVO_4$. Element mapping images based on high-angle annular dark field scanning transmission electron microscopy (HAADF-STEM, Fig. S4) display that all the Bi, V and O elements are homogeneously distributed over q-$BiVO_4$, and the quantitative estimation by energy dispersive X-ray (EDX) spectroscopy presents the stoichiometric composition of Bi, V and O elements in q-$BiVO_4$ (Fig. S5).

Photocatalytic performance. The photocatalytic CH_4 oxidation was investigated in a high-pressure stainless-steel vessel with a transmittance quartz glass window on the top plate (Fig. S6). The adoption of high-pressure reactor is based on below two considerations. One is to economically utilize the available pressure energy from the practical transportation and storage condition of natural gas, where the pressure is as high as 70-200 bar in main pipelines and tanks[20, 21]. The specific analysis is briefly summarized in supplementary information (Fig. S7). The other is to promote the yield of desired products through dissolving more CH_4 reactants in the solvent at high pressure. In a typical reaction, 10 mg q-

$BiVO_4$ photocatalysts were dispersed in certain amount of H_2O, while the total pressure of CH_4 and O_2 mixed gas was fixed to be 20 bar. After irradiation with Hg lamp (excitation wavelength of 300-600 nm) at room temperature (surface temperature of catalyst = 28.5±0.5^oC, Fig. S8), the yield of liquid organic products such as CH_3OH and C_2H_5OH was evaluated by nuclear magnetic resonance spectroscopy (NMR) and gas chromatography (GC) with flame ionization detector. Note that liquid HCHO is known to exist in the form of methanediol ($HOCH_2OH$) in aqueous solution[22], which ^1H NMR signal overlaps with the broad peak of water solvent. So, the quantity of HCHO was determined by acetylacetone color-developing method (Fig. S9, S10, S11). Other gaseous products (CO_2, C_2H_6, O_2 and H_2) were monitored by GC spectra with flame ionization and thermal conductivity detectors.

The effect of photocatalyst type, O_2 and H_2O amount, reaction time, irradiation wavelength as well as light intensity on CH_4 conversion performance is investigated in detail. First of all, photocatalytic activity of q-$BiVO_4$ (4.5 nm) is compared with conventional s-$BiVO_4$ (454.3 nm, Fig. S12). As shown in Fig. 3a, about 4 folds in the oxygenated products by q-$BiVO_4$ (2.3 mmol g^{-1} CH_3OH, 1.9 mmol g^{-1} HCHO and 0.3 mmol g^{-1} CO_2) are acquired with respect to s-$BiVO_4$ (0.5 mmol g^{-1} CH_3OH, 0.5 mmol g^{-1} HCHO and 0.1 mmol g^{-1} CO_2). The corresponding increment is also distinguished in conversion of CH_4 and O_2 reactants (Fig. S13a). These enhancements by q-$BiVO_4$ are ascribed to both the raised charge carrier kinetics (Fig. S14) and the improved Brunauer-Emmett-Teller (BET) specific surface area (226.9 m^2 g^{-1}, Fig. S15). This deduction is supported by comparing the BET surface area normalized CH_4 oxidation activity (Table S1), and q-$BiVO_4$ still exhibits higher performance than s-$BiVO_4$. Except for s-$BiVO_4$, commercial TiO_2 nanoparticle (P25) is also employed as the contrast sample and tested under the same reaction condition, and only HCHO (48.9 μmol g^{-1}) and CO_2 (48.9 μmol g^{-1}) are found in the products (Fig. S16).

Optimizing the yield of both CH_3OH and HCHO is carried out through varying O_2 amount (Fig. 3b)[12, 23]. The highest productivity of CH_3OH and HCHO is 2.3 and 1.9 mmol g^{-1} at the O_2 pressure of 10 bar, respectively, and the corresponding conversion percentage of O_2 is 0.23% (Fig. S13b). The gradual increase of oxygenates at the O_2 partial pressure of less than 10 bar implies that O_2 involves the rate-determining step of CH_4 oxidation. When the O_2 pressure surpasses 10 bar, the reduced productivity of CH_3OH and HCHO is ascribed to the lowered CH_4 partial pressure and their overoxidation to CO_2. Hence, the partial pressure of O_2 is controlled to be 10 bar.

The inspection of reaction time discloses that 3 h is the best for the yield of CH_3OH (2.3 mmol g^{-1}) though its selectivity continuously decreases (Fig. 3c). It is noticed that when the reaction time arrives 7 h, the productivity of HCHO ascends to 5.6 mmol g^{-1} with 69.8% selectivity, demonstrating that the prolonged reaction promotes oxidation of both CH_4 reactants and CH_3OH intermediates. The corresponding conversion percentage of CH_4 at 7 h is 0.40% (Fig. S13c) with turnover number (TON) of 2.6. Evidently, extending the reaction time enables improving the HCHO selectivity simultaneously ensuring its output.

The balance between the consumption rate of feed gas (CH_4 and O_2) and the formation rate of products (CH_3OH, HCHO and CO_2) is explored by Fig. S17 and S18.

H_2O acts as the solvent for CH_4 oxidation. Fig. 3d shows that with the H_2O volume increase from 10 to 80 mL, conversion of CH_4 and O_2 synchronously improves from 0.23% (TON = 1.5) to 0.54% (TON = 3.5) (Fig. S13d), while the yield of CH_3OH and HCHO gets to 6.8 and 4.0 mmol g^{-1}, respectively. More CH_4 molecules are dissolved in aqueous solution with H_2O amount increasing, leading to the rise of CH_3OH product. Moreover, the concentration of CH_3OH is diluted in a large volume of H_2O, alleviating overoxidation to HCHO and CO_2 and causing enhancement of the selectivity towards CH_3OH. It is noted that owing to the possible test error in low concentration of CH_3OH solution (Fig. S19), further increase of H_2O volume is not tried. Nevertheless, augmenting the solvent volume is an efficient method to boost the selectivity of CH_3OH with high yield.

The relationship between photocatalytic performance and input photon number or light energy is also examined. As indicated in Fig. 3e, along with the increase of light intensity of Hg lamp, the yield of CH_3OH, HCHO and CO_2 all raises from 1.0 (CH_3OH, 100 mW cm^{-2}), 0.5 (HCHO, 100 mW cm^{-2}) and 0.2 (CO_2, 100 mW cm^{-2}) to 2.3 (CH_3OH, 170 mW cm^{-2}), 1.9 (HCHO, 170 mW cm^{-2}) and 0.3 mmol g^{-1} (CO_2, 170 mW cm^{-2}), respectively. This result manifests that the photocatalytic CH_4 conversion largely depends on the inputted photon number. Fig. 3f and Table S2 further summarize the photocatalytic efficiency under irradiation of monochromatic light with different energy. In good agreement with change in the diffuse reflectance spectrum, the quantum efficiency (Q.E.) value of q-$BiVO_4$ (0, 0, 0.47, 0.82 and 3.07%) increases with the reduction of irradiation light wavelength (630, 535, 470, 420 and 365 nm). The prominent photon utilization efficiency of 3.07% at 365 nm demonstrates that irradiation with the short-wavelength and high-energy light would promote the oxidation conversion of CH_4. The quantitative conversion percentage of CH_4 and O_2 is outlined in Fig. S13e and S13f.

Based on the above results, we conclude the favorable reaction condition for production of HCHO and CH_3OH, respectively. Since HCHO is the further oxidation product of CH_3OH, increasing the oxidation capacity would be an efficient strategy to elevate the selectivity of HCHO. As demonstrated in Fig. 4a, utilization of short-wavelength UV irradiation (300-400 nm) with high intensity (170 mW cm^{-2}) not only promotes the CH_4 conversion but also accelerates the oxidation of CH_3OH to HCHO. Significantly, upon a long time oxidation of 7 h, HCHO product is achieved with a good selectivity and yield of 86.7% and 13.1 mmol g^{-1} (TON = 4.7), respectively. The corresponding conversion of both CH_4 and O_2 reaches 0.73% (Fig. S13g). On the contrary, reducing the oxidation degree of reaction system could be conducive to production of CH_3OH. Using visible Xenon lamp irradiation (400-780 nm), a remarkable 92.8% selectivity of CH_3OH is achieved in 10 mL H_2O. It needs to be pointed out that the weak oxidation capacity under visible light inevitably results in low productivity of oxygenates. Therefore, by increasing the dissolved CH_4 in 80 mL H_2O, the yield of CH_3OH is promoted to 1.1 mmol g^{-1} with an exceptional selectivity of

96.6% (TON = 0.4, Fig. 4b, S20). The corresponding conversion of both CH_4 and O_2 is 0.06% (Fig. S13h). Evidently, the diluted concentration of CH_3OH generated in large solvent volume gives rise to the enhanced selectivity from 92.8% to 96.6% through depressing the overoxidation (Fig. S21). The contrast experiments with absence of catalyst, CH_4, O_2 or H_2O show no production of oxygenates under visible light irradiation (Table S3). To preclude the influence of temperature, thermocatalytic reaction (30^oC) under similar condition is also conducted and no products is observed (Fig. S22). It deserves to be stressed that the highly selective generation of CH_3OH or HCHO from CH_4 oxidation over the single photocatalyst is unattained in previous works (Table S4).

Photocatalytic mechanism. Fig. 5A illustrates the proposed radical mechanism for CH_4 oxidation on q-$BiVO_4$ (Fig. 5). Under light irradiation, q-$BiVO_4$ is excited to induce $^{\bullet}OH$ generation via two routes: oxidation of H_2O by valence band holes and reduction of O_2 by conduction band electrons (step 1). The $^{\bullet}OH$ cleaves C-H bond for producing the methyl radical ($^{\bullet}CH_3$) (step 2), which is a rate-determining step. Also as an oxidant, O_2 rapidly binds to $^{\bullet}CH_3$ and then reacts with as-formed H^+ and electron to generate methylhydroperoxide (CH_3OOH, step 3), which will be reduced by electrons[23, 24] or decomposed under UV irradiation to form CH_3OH (step 4)[25, 26]. Upon oxidation by holes from valence band of q-$BiVO_4$, as-formed CH_3OH is further activated to $^{\bullet}CH_2OH$ that is combined with $^{\bullet}OH$ to produce HCHO in the form of $HOCH_2OH$ (step 5). In the following parts, we validate this reaction mechanism step by step.

To solidly prove that the oxygenated products results from the conversion of CH_4, $^{13}CH_4$ was used as reactant instead of $^{12}CH_4$. Gas chromatography-mass spectrometry (GC-MS) with isotopically labelled $^{13}CH_4$ discloses that CH_4 is the carbon source of CH_3OH with the appearance of $^{13}CH_3OH$ peak at m/z = 33 (red curve in Fig. 6a). The obvious ^{13}C NMR peaks of CH_3OH and $HOCH_2OH$ (HCHO) also verify that the C1 oxygenated products are derived from CH_4 (black curve in Fig. S23a). The carbon type of C1 oxygenated products is identified from the ^{13}C DEPT-135 (distortionless enhancement by polarization transfer) spectrum, where up and down signals represent -CH_3 and -CH_2 groups from CH_3OH and $HOCH_2OH$ (HCHO), respectively (red curve in Fig. S23a). Furthermore, as displayed in Fig. S23b, satellite peaks of $^{13}CH_3OH$ (δ = 3.12 and 3.40 ppm) are discerned in ^1H NMR spectrum without $^{12}CH_3OH$ (δ = 3.28 ppm) signal[23], indicating that CH_4 is the 100% carbon source for CH_3OH product. Similarly, 2D ^1H-^{13}C HMQC (heteronuclear multiple-quantum correlation, Fig. S24) and 2D ^1H-^{13}C HMBC (heteronuclear multiple-bond correlation, Fig. S25) spectra indicate that $^{13}CH_4$ is the feedstock for HCHO ($HOCH_2OH$) generation.

According to the mechanism illustration, $^{\bullet}OH$ is responsible for removing the H atom from CH_4 molecule, which is the key step for CH_4 activation. To explore the ability of q-$BiVO_4$ towards the generation of $^{\bullet}OH$ in step 1, its band structure is established through UV-Vis diffuse reflectance spectrum[27] (Fig. S26a), transformed Kubelka-Munk function plot (Fig. S26b)[28], Mott-Schottky plot (Fig. S26c, S27)[29] and

ultraviolet photoelectron spectroscopy (Fig. S28). As shown in Fig. 6b, the conduction and valence bands of q-$BiVO_4$ are tested to be 0.075 and 2.555 V *vs.* normal hydrogen electrode (NHE) at pH=0, respectively. Therefore, the $^{\bullet}OH$ can be produced through two approaches: H_2O oxidation ($^{\bullet}OH/H_2O$: 2.380 eV *vs.* NHE at pH=0)[30] and two-electron O_2 reduction ($O_2/^{\bullet}OH$: 0.695 eV *vs.* NHE at pH=0)[31]. In order to assess the generation of $^{\bullet}OH$ from both hole oxidation and electron reduction of q-$BiVO_4$, we carried out the fluorescence detection of coumarin solution without or with O_2 (Fig. S29). In the absence of O_2 (Fig. S29a), an enhanced fluorescence signal is achieved with q-$BiVO_4$ photocatalyst under visible light, indicating that the holes from valence band can successfully oxidize H_2O into $^{\bullet}OH$. After the solution is saturated with O_2 (Fig. S29b), the fluorescence intensity with q-$BiVO_4$ exhibits 2.3 times increase than that in absence of O_2, confirming that O_2 also greatly contributes to the generation of $^{\bullet}OH$. Note that the quantity of O_2 solely generated from H_2O decomposition by q-$BiVO_4$ is too low to make a detectable yield of oxygenates (Fig. S30). Moreover, the energy band structure of s-$BiVO_4$ is likewise constructed (Fig. S31 and S32) with the conduction and valence bands at 0.084 and 2.474 V *vs.* NHE at pH=0, respectively. With respect to the energy band structure of s-$BiVO_4$, the more negative conduction band and positive valence band of q-$BiVO_4$ lead to more $^{\bullet}OH$ species for CH_4 oxidation (Fig. S33). We notice that such fluorescence signal comes from 7-hydroxycoumarin that is the $^{\bullet}OH$ trapping product of coumarin (Fig. S34 and S35).

Step 2 refers to the activation step of CH_4 by $^{\bullet}OH$, which is recognized as the rate-determining step in this work. To verify that $^{\bullet}OH$ is the initiator for CH_4 activation on the surface of q-$BiVO_4$ rather than the photoinduced hole, we performed a thermocatalytic reaction containing 10 mg q-$BiVO_4$, 5 mL H_2O_2, 5 mL H_2O, 10 bar O_2 and 10 bar CH_4 at 60^{o}C in absence of light irradiation. The H_2O_2 is decomposed to provide $^{\bullet}OH$ at 60^{o}C, and the dark condition prevents the hole formation on the surface of q-$BiVO_4$. After reaction, CH_4 is found to be oxidized to CH_3OOH, which is not further reduced to CH_3OH due to the lack of photogenerated electrons under dark condition (Fig. 6c). In absence of H_2O_2 (Fig. S36) or q-$BiVO_4$ (Fig. 6d), no oxygenated product is distinguished. Thus, we deduce that $^{\bullet}OH$ activates CH_4 for oxygenate generation on the surface of q-$BiVO_4$. Besides, the solid evidence that CH_4 is not directly oxidized by photoinduced holes from q-$BiVO_4$ is supported by electron spin resonance (ESR) spectroscopy (Fig. 6e). Under Xenon lamp irradiation in argon (Ar) atmosphere, the ESR spectrum of q-$BiVO_4$ shows a g value of 2.006[32], corresponding to the active hole center O^- (Fig. 6e, blue curve); subsequently, atmosphere is switched from Ar to CH_4, no distinct intensity decrease is discerned on O^- signal (Fig. 6e, green curve), indicating no occurrence of reaction between O^- hole and CH_4 molecule[33]; on the contrary, upon continuous irradiation for 15 min in CH_4 atmosphere, the intensity of O^- signal increases (Fig. 6e, red curve), again denying that the O^- hole can directly oxidize CH_4. The fact that C-H bond breakage is rate-determining step of CH_4 oxidation was verified through kinetic isotope effect (KIE)[34]. Taking 420 nm monochromatic light for irradiation, the KIE value is estimated to be 8.3 (larger than 6)[35] based on the

reaction rate ratio (k_H / k_D) using CH_4 or CD_4 as reactants, respectively (Fig. 6f and S37). This large value reveals the C-H bond cleavage in the rate-determining step.

Incorporation of O_2 with $^{\bullet}CH_3$ to form CH_3OH in step 3 was proved by $^{18}O_2$ and $H_2{}^{18}O$ isotope tests as well as the reusability of q-$BiVO_4$ photocatalyst, considering that these three oxygen sources possibly involved the catalytic reaction. GC-MS analyses (Fig. 6g) demonstrate that $CH_3{}^{18}OH$ fragment occupies 100% intensity by using $^{18}O_2$ and $H_2{}^{16}O$, whereas the $CH_3{}^{16}OH$ fragment contains 100% intensity by using $^{16}O_2$ and $H_2{}^{18}O$. Therefore, one can deduce that the O element in H_2O is not incorporated into CH_3OH formation during the photocatalytic CH_4 oxidation. To exclude the possibility of lattice O in q-$BiVO_4$ as oxygen source, its stability was evaluated. After five photocatalytic cycles, q-$BiVO_4$ almost preserves its initial catalytic activity (Fig. S38). Therefore, O_2 is the mere oxygen source for CH_3OH formation (step 3). TEM images (Fig. S39), XRD patterns (Fig. S40), XPS (Fig. S41), Raman (Fig. S42a), UV-Vis diffuse reflectance spectra (Fig. S42b) and inductively coupled plasma optical emission spectrometer tests (Fig. S43) were carried out to prove only slight change in the morphologies and chemical states of q-$BiVO_4$ before and after photocatalytic reaction.

According to step 4, CH_3OOH is first formed and then reduced to CH_3OH. Since this reduction process easily happens under high photoinduced electron density[36], the NMR signal of CH_3OOH is difficult to be detected. Therefore, we increased the amount of q-$BiVO_4$ (50 mg) and reduced the amount of H_2O solvent (0.5 mL) in order to increase the concentration of CH_3OOH intermediates. By prolonging the reaction time to 7 h, a weak CH_3OOH peak appeared at 3.78 ppm, providing the clear evidence on CH_3OOH production (Fig. 6h). As-formed CH_3OH would be further oxidized to HCHO ($HOCH_2OH$) in step 5. Based on the Gibbs free energy values (Fig. 1)[22, 37, 38], oxidation of CH_3OH to HCHO is thermodynamically favorable. To confirm this transformation process from the experimental aspect, CH_3OH was taken as reactants in a similar photocatalytic system with argon (Ar) replacing CH_4. The ^{13}C NMR spectrum of CH_3OH oxidation products verifies that CH_3OH can be oxidized to $HOCH_2OH$ using q-$BiVO_4$ as catalysts under light illumination (Fig. S6i).

Summary

Through regulation of reaction time, irradiation wavelength, light intensity and the adding amount of O_2 as well as H_2O, selective oxidation of CH_4 into CH_3OH and HCHO with satisfied yield is successfully realized over q-$BiVO_4$ photocatalyst at room temperature under the aerobic condition. The quantum sized q-$BiVO_4$ with an appropriate energy band structure enables simultaneous H_2O oxidation via photogenerated holes and O_2 reduction via photogenerated electrons, greatly promoting the production of $^{\bullet}OH$. As-formed $^{\bullet}OH$ causes the cleavage of C-H bond in CH_4 and gives to the generation of $^{\bullet}CH_3$, which is proved to be a rate-determining step. Except for participating into $^{\bullet}OH$ production, O_2 is found to incorporate with $^{\bullet}CH_3$, resulting in the oxygenated products. This work not only provides a comprehensive

analysis for CH_4 oxidation, but also broadens the avenue toward selective conversion of CH_4 into valuable products in sustainable way.

Methods

Chemicals. Bismuth nitrate pentahydrate ($Bi(NO_3)_3·5H_2O$), ammonium metavanadate (NH_4VO_3), coumarin, deuteroxide (D_2O), water-^{18}O ($H_2{}^{18}O$), barium sulfate ($BaSO_4$) and dimethyl sulfoxide (DMSO) were all purchased from Innochem in Beijing. LUDOX® HS-40 colloidal silica 40 wt.% suspension in water was bought from Sigma-Aldrich. Gases of CH_4 and O_2 were achieved from KODI corporation in Foshan. Isotopic gases of $^{18}O_2$, $^{13}CH_4$ and CD_4 were obtained from LION biology corporation in Shanghai. All the chemicals were used as received without further purification. Deionized water with a resistivity of 18.2 MΩ cm^{-1} was used in all experiments.

Photocatalyst preparation. The q-$BiVO_4$ was prepared through a template method. 0.48 g $Bi(NO_3)_3·5H_2O$ was dissolved in 10 mL 1 M HNO_3, meanwhile 0.12 g NH_4VO_3 was added into another 15 mL HNO_3 solution, giving two precursor solutions with concentration of 1 mM, respectively. Under vigorous stirring, two precursor solutions were mixed with silica gel (12 nm in diameter) added as the template. After rotary evaporation drying, the prepared powder was calcinated at 400^oC to obtain $BiVO_4$-silica composite. As for silica template removal, 70 mg $BiVO_4$-silica composite was dispersed in 70 mL deionized water by ultrasonication. Then, the suspension was transferred into a 100 mL Teflon-lined stainless-steel autoclave, which was treated under hydrothermal reaction at 180^oC for 24 h. Finally, q-$BiVO_4$ was obtained by centrifugation and dried at 60^oC for 12 h.

The s-$BiVO_4$ with an average size of 454.3 nm was synthesized by a standard precipitation method. Typically, 2.9 g $Bi(NO_3)_3·5H_2O$ and 0.69 g NH_4VO_3 were dissolved in 25 mL 2 mM HNO_3 solution, and the solution was stirred until clear. Then, 5 g urea was added into the mixed solution followed by heating at 90^oC for 24 h under continuous stirring. The product was washed thoroughly with pure water and drying at 60^oC overnight.

Characterization. Transmission electron microscopy (TEM), high-resolution TEM (HRTEM), selected area electron diffraction (SAED), high-angle annular darkfield scanning transmission electron microscopy (HAADF-STEM), elemental mapping and energy dispersive X-ray (EDX) spectroscopy were carried out on a FEI Tecnai G2 F20 electron microscope operated at 200 kV. Scanning electron microscopy (SEM) was performed on a Hitachi S8220 scanning electron microscope. The crystal structures were characterized through power X-ray diffraction patterns (XRD), which were carried out on D/MAX-TTRIII (CBO) and Xeuss SAXS/WAXS system with Cu Kα radiation (λ = 1.542 Å) operating at 50 kV and 300 mA. UV-Vis diffuse reflectance spectra taking $BaSO_4$ as internal reference sample were recorded on a Hitachi U-3010 UV-Vis spectrometer. A Mott-Schottky plot was performed on CHI 760E electrochemical workstation in 1 M Na_2SO_4 solution under frequencies of 500, 700 and 900 Hz, respectively.

Photocatalytic oxidation of CH_4. Photocatalytic oxidation of CH_4 was performed in a stainless-steel autoclave with a quartz glass window on the top (Supplementary Fig. S5). Photocatalysis experiments were carried out at a fixed pressure of 20 bar and room temperature along with 25^oC cooling water unless otherwise stated. 10 mg photocatalyst sample was placed at the center inside reactor, and then certain amount of deionized water was added. The mixed CH_4 and O_2 at different ratio (8:12, 10:10, 12:8, 14:6) were filled, and high-pressure mercury lamp (excitation wavelength of 300-600 nm, CEAULIOHT), Xenon lamp (excitation wavelength of 400-780 nm and irradiation intensity of 170 mW cm^{-2}, Perfect Light) or LED monochromatic light source (Perfect Light) was used the light source for photocatalytic reactions.

Thermocatalytic oxidation of CH_4 in presence of H_2O_2. To verify that $^{\bullet}OH$ activated CH_4 for CH_3OH formation on the surface of q-$BiVO_4$, a free radical based thermocatalytic reaction was performed at 60^oC. 10 mg q-$BiVO_4$ was dispersed in the mixture of 5 mL H_2O_2 and 5 mL H_2O. 10 bar O_2 and 10 bar CH_4 were charged to make a total gas pressure to be 20 bar. Under dark condition, the reaction system was heated to 60^oC.

Product analysis. Analysis of the C1 oxygenated liquid product (CH_3OOH, CH_3OH, HCHO) was carried out using GC, GC-MS, and NMR spectroscopy. GC equipped with a flame ionization detector was performed on Shimadzu GC-2014C to analyze and quantify the product of CH_3OH. A Shimadzu GC-MS QP2010 Ultra was applied to monitor generation of $^{13}CH_3OH$. The ^{1}H-NMR, ^{13}C-NMR, ^{13}C DEPT-135, 2D ^{1}H-^{13}C HMQC and 2D ^{1}H-^{13}C HMBC were recorded on Bruker AVANCE III HD 400 MHz nuclear magnetic resonance spectrometer. The amount of HCHO was quantified with acetylacetone color-developing method.

Acetylacetone color-developing method. 3 mL product solution was mixed with 2 mL as-prepared 0.25% (V/V) acetylacetone solution, and then heated for 3 min in boiling water. Afterward, the mixed solution became yellow-color. Through absorbance detection at 413 nm, the HCHO content was obtained. Specific reaction mechanism was shown in Fig. S6.

Preparation of 0.25% (V/V) acetylacetone solution. 25 g ammonium acetate was dissolved in 10 mL water, and then 3 mL acetic acid and 0.25 mL acetylacetone were added in sequence. Afterward, the solution volume was diluted to 100 mL. With pH adjusted to 6, the solution was stored at 2^oC - 5^oC, which could stay stable for one month.

Band structure establishment of q-$BiVO_4$. Taking $BaSO_4$ as internal reference sample, the UV-Vis diffuse reflectance spectrum of q-$BiVO_4$ was recorded on a Hitachi U-3010 UV-Vis spectrometer. For Mott-Schottky test, 5 mg q-$BiVO_4$ was ultrasonically dispersed in 1 mL mixed solution (0.2 mL ethanol + 0.8 mL water), and then dropped onto three 1 cm × 1 cm sized indium tin oxide (ITO) substrates as electrodes. Taking Ag/AgCl as reference electrode and Pt wire mesh as counter electrode, the Mott-Schottky plots were tested on CHI 760E electrochemical workstation in 1 M Na_2SO_4 solution under frequencies of 500, 700 and 900 Hz, respectively. The valence band of q-$BiVO_4$ was tested through ultraviolet photoelectron spectroscopy (UPS). The UPS spectrum was carried out on an EscaLab 250Xi.

The sample was pressed into film and bonded to the surface of conductive tape, while the other surface of conductive tape was fixed on the stage. Electrical contact between the stage and sample was made using a copper tape. Subsequently, the sample was stored within a vacuum chamber for further test. During the UPS measurement, He(I) emission line provided an illumination at 21.22 eV from a helium discharge lamp, and the partial gas pressure of He was adjusted to 2×10^{-8} mbar. The stage was biased at -10.0 eV in order to accurately guarantee the low-kinetic energy cutoff and the collection of electron emission at 0^{o} from normal. Cutoff energy was measured from the intersection between the linear extrapolation of the cutoff region and the baseline.

Hydroxyl radical detection. Coumarin was taken as a probe to detect production of $^{\bullet}OH$ through monitoring formation of 7-OH-coumarin. Typically, 8 mg photocatalyst was dispersed in 15 mL 1 mM coumarin aqueous solution under stirring, and then either argon gas was injected to evacuate the air to produce an anaerobic environment or O_2 was bubbled to create a saturated O_2 condition under the sealed condition. After irradiation for 1 h, a certain amount of reaction solution was taken out and centrifuged to examine the fluorescence spectrum.

Plasma optical emission spectrometer tests (ICP-OES). In order to investigate the dissolved amount of catalysts, ICP-OES test on Bi element was conducted on the solution before and after photocatalytic reaction. 10 mg q-$BiVO_4$ was dispersed into 10 mL H_2O with stirring for 3 h under dark condition. Through centrifugation, the aqueous solution was collected as sample 1. Meanwhile, the other 10 mg q-$BiVO_4$ was dispersed into 10 mL H_2O, following by charging with 10 bar CH_4 and 10 bar O_2. After photocatalytic reaction for 3 h with stirring, the aqueous solution was obtained through centrifugation, denoted as sample 2. Both samples were tested by ICP-OES to check the dissolved catalyst during reaction. The corresponding ICP-OES test was carried out on Thermo Scientific iCAP6300 with CID detector.

Electron spin resonance (ESR). ESR spectroscopy was used to determine if CH_4 was directly oxidized by photoinduced holes from q-$BiVO_4$. Under Xenon lamp irradiation, the ESR spectra of q-$BiVO_4$ were recorded at 9.43 GHz and a liquid nitrogen temperature (77 K) using a Bruker EMX spectrometer under Ar or CH_4 atmosphere.

Kinetic isotope effect (KIE) test. Typically, 10 mg q-$BiVO_4$ was dispersed in 10 mL H_2O, and then 10 bar CH_4 (or CD_4) and 10 bar O_2 were charged into vessel. The monochromatic 420 nm light (100 mW cm^{-2}) was employed for irradiation, while 25°C cooling water was used to keep the reaction at room temperature. After reaction for 3, 5 or 7 h, the yield of oxygenates (CH_3OH, HCHO and CO_2) was tested from CH_4 and CD_4 reactant systems, respectively. According to the corresponding yield under different reaction time, we calculated the product formation rate constant in CH_4 (k_H) and CD_4 (k_D) systems, respectively. As a result, the rate-determining step was verified through KIE = k_H / k_D.

Date availability. The data that support the findings within this study are available upon request.

Declarations

Acknowledgements

This work was sponsored by China Postdoctoral Science Foundation (2018M643041), “Strategic Priority Research Program” of Chinese Academy of Sciences (XDA09040100, Z.Y.T.), National Key Basic Research Program of China (2016YFA0200700, Z.Y.T.), Frontier Science Key Project of Chinese Academy of Sciences (QYZDJ-SSW-SLH038, Z.Y.T.), National Natural Science Foundation of China (21890381 and 21721002, Z.Y.T.), and K.C. Wong Education Foundation (Z.Y.T.). The authors also thank Yanan Shi and Wenshi Zhao for laboratory support as well as Institute of Chemistry Chinese Academy of Sciences for hosting partial NMR tests.

Author contributions

Y.F. and Z.T. conceived the idea, developed the outline, designed the experiment and compiled the manuscript. Y.F. conducted all the experiments and tests with the assistance of W.Z., X.Q., H.L. Y.J. and Z.S. D.H. coordinated the project and provided critical feedback. L.N. and Z.T. supervised the whole project.

Competing interests

The authors declare no competing interests.

References

1. Ravi M, Ranocchiari M, Van Bokhoven JA. The Direct Catalytic Oxidation of Methane to Methanol—A Critical Assessment. *Angew. Chem. Int. Ed.* **56**, 16464-16483 (2017).
2. Hu W, Lan J, Guo Y, Cao X-M, Hu P. Origin of Efficient Catalytic Combustion of Methane over Co_3O_4(110): Active Low-Coordination Lattice Oxygen and Cooperation of Multiple Active Sites. *ACS Catal.* **6**, 5508-5519 (2016).
3. Aoki K, et al. Direct conversion of methane into methanol over MoO_3/SiO_2 catalyst in an excess amount of water vapor. *Catal. Today* **45**, 29-33 (1998).
4. Sugino T, Kido A, Azuma N, Ueno A, Udagawa Y. Partial Oxidation of Methane on Silica-Supported Silicomolybdic Acid Catalysts in an Excess Amount of Water Vapor. *J. Catal.* **190**, 118-127 (2000).
5. Tang P, Zhu Q, Wu Z, Ma D. Methane activation: the past and future. *Energy & Environ Sci.* **7**, 2580-2591 (2014).
6. Sushkevich VL, Palagin D, Ranocchiari M, van Bokhoven JA. Selective anaerobic oxidation of methane enables direct synthesis of methanol. *Science* **356**, 523-527 (2017).
7. Tomita A, Nakajima J, Hibino T. Direct Oxidation of Methane to Methanol at Low Temperature and Pressure in an Electrochemical Fuel Cell. *Angew. Chem. Int. Ed.* **120**, 1484-1486 (2008).

8. Zhou Y, Zhang L, Wang W. Direct functionalization of methane into ethanol over copper modified polymeric carbon nitride via photocatalysis. *Nat. Commun.* **10**, 506-513 (2019).
9. Xie J, et al. Highly selective oxidation of methane to methanol at ambient conditions by titanium dioxide-supported iron species. *Nat. Catal.* **1**, 889-896 (2018).
10. Murcia-López S, Villa K, Andreu T, Morante JR. Partial Oxidation of Methane to Methanol Using Bismuth-Based Photocatalysts. *ACS Catal.* **4**, 3013-3019 (2014).
11. Taylor CE. Methane conversion via photocatalytic reactions. *Catal. Today* **84**, 9-15 (2003).
12. Song H, et al. Direct and Selective Photocatalytic Oxidation of CH_4 to Oxygenates with O_2 on Cocatalysts/ZnO at Room Temperature in Water. *J. Am. Chem. Soc.* **141**, 20507-20515 (2019).
13. Michael D. Ward JFB. Methane Photoactivation on Copper Molybdate. An Experimental and Theoretical Study. *J. Phys. Chem.* **91**, 6515-6521 (1987).
14. J. Xin XC, J. Suo, Xia. Zhang, L. Yan and Shuben Li. Nb- and Ti-containing silica-based mesoporous molecular sieves as catalysts for photocatalytic oxidation of methane. *Stud. Surf. Sci. Catal.* **135**, 1 (2001).
15. Bañares MA, Alemany LJ, López Granados M, Faraldos M, Fierro JLG. Partial oxidation of methane to formaldehyde on silica-supported transition metal oxide catalysts. *Catal. Today* **33**, 73-83 (1997).
16. Yuliati L, Yoshida H. Photocatalytic conversion of methane. *Chem. Soc. Rev.* **37**, 1592-1602 (2008).
17. Bahmanpour AM, Hoadley A, Tanksale A. Formaldehyde production via hydrogenation of carbon monoxide in the aqueous phase. *Green Chem.* **17**, 3500-3507 (2015).
18. Zalfani M, Mahdouani M, Bourguiga R, Su BL. Experimental and theoretical study of optical properties and quantum size phenomena in the $BiVO_4/TiO_2$ nanostructures. *Superlattice. Microstruct.* **83**, 730-744 (2015).
19. Venkatesan R, Velumani S, Kassiba A. Mechanochemical synthesis of nanostructured $BiVO_4$ and investigations of related features. *Mater. Chem. Phys.* **135**, 842-848 (2012).
20. Kumar S*, et al.* LNG: An eco-friendly cryogenic fuel for sustainable development. *Appl. Energ.* **88**, 4264-4273 (2011).
21. Dispenza C, Dispenza G, La Rocca V, Panno G. Exergy recovery during LNG regasification: Electric energy production – Part one. *Appl. Therm. Eng.* **29**, 380-387 (2009).
22. Hahnenstein I, Hasse H, Kreiter CG, Maurer G. ^{1}H- and ^{13}C-NMR-Spectroscopic Study of Chemical Equilibria in Solutions of Formaldehyde in Water, Deuterium Oxide, and Methanol. *Ind. Eng. Chem. Res.* **33**, 1022-1029 (1994).
23. Agarwal N, et al. Aqueous Au-Pd colloids catalyze selective CH_4 oxidation to CH_3OH with O_2 under mild conditions. *Science* **358**, 223-227 (2017).
24. Cui X, et al. Room-Temperature Methane Conversion by Graphene-Confined Single Iron Atoms. *Chem* **4**, 1902-1910 (2018).
25. Vaghjiani GL, Ravishankara AR. Absorption cross sections of CH_3OOH, H_2O_2, and D_2O_2 vapors between 210 and 365 nm at 297 K. *J. Geophys. Res.* **94**, 3487-3492 (1989).

26. Roehl CM, Marka Z, Fry JL, Wennberg PO. Near-UV photolysis cross sections of CH_3OOH and $HOCH_2OOH$ determined via action spectroscopy. *Atmos. Chem. Phys.* **7**, 713-720 (2007).
27. Sun S, Wang W, Li D, Zhang L, Jiang D. Solar Light Driven Pure Water Splitting on Quantum Sized $BiVO_4$ without any Cocatalyst. *ACS Catal.* **4**, 3498-3503 (2014).
28. Zhang N, et al. Monoclinic Tungsten Oxide with {100} Facet Orientation and Tuned Electronic Band Structure for Enhanced Photocatalytic Oxidations. *ACS Appl. Mater. Inter.* **8**, 10367-10374 (2016).
29. Wang L, Han D, Ni S, Ma W, Wang W, Niu L. Photoelectrochemical device based on Mo-doped $BiVO_4$ enables smart analysis of the global antioxidant capacity in food. *Chem. Sci.* **6**, 6632-6638 (2015).
30. Nosaka Y, Nosaka AY. Generation and Detection of Reactive Oxygen Species in Photocatalysis. *Chem. Rev.* **117**, 11302-11336 (2017).
31. Jiang J, Li H, Zhang L. New Insight into Daylight Photocatalysis of AgBr@Ag: Synergistic Effect between Semiconductor Photocatalysis and Plasmonic Photocatalysis. *Chem. Eur. J.* **18**, 6360-6369 (2012).
32. Sterrer M, Diwald O, Knözinger E, Sushko PV, Shluger AL. Energies and Dynamics of Photoinduced Electron and Hole Processes on MgO Powders. *J. Phy.s Chem. B* **106**, 12478-12482 (2002).
33. Kaliaguine SL, Shelimov BN, Kazansky VB. Reactions of methane and ethane with hole centers O^-. *J. Catal.* **55**, 384-393 (1978).
34. Simmons EM, Hartwig JF. On the Interpretation of Deuterium Kinetic Isotope Effects in C-H Bond Functionalizations by Transition-Metal Complexes. *Angew. Chem. Int. Ed.* **51**, 3066-3072 (2012).
35. Gómez-Gallego M, Sierra MA. Kinetic Isotope Effects in the Study of Organometallic Reaction Mechanisms. *Chem. Rev.* **111**, 4857-4963 (2011).
36. Anglada JM, Crehuet R, Martins-Costa M, Francisco JS, Ruiz-López M. The atmospheric oxidation of CH_3OOH by the OH radical: the effect of water vapor. *Phys. Chem. Chem. Phys.* **19**, 12331-12342 (2017).
37. Meng X, Cui X, Rajan NP, Yu L, Deng D, Bao X. Direct Methane Conversion under Mild Condition by Thermo-, Electro-, or Photocatalysis. *Chem* **5**, 2296-2325 (2019).
38. Hahnenstein I, Albert M, Hasse H, Kreiter CG, Maurer G. NMR Spectroscopic and Densimetric Study of Reaction Kinetics of Formaldehyde Polymer Formation in Water, Deuterium Oxide, and Methanol. *Ind. Eng. Chem. Res.* **34**, 440-450 (1995).

Figures

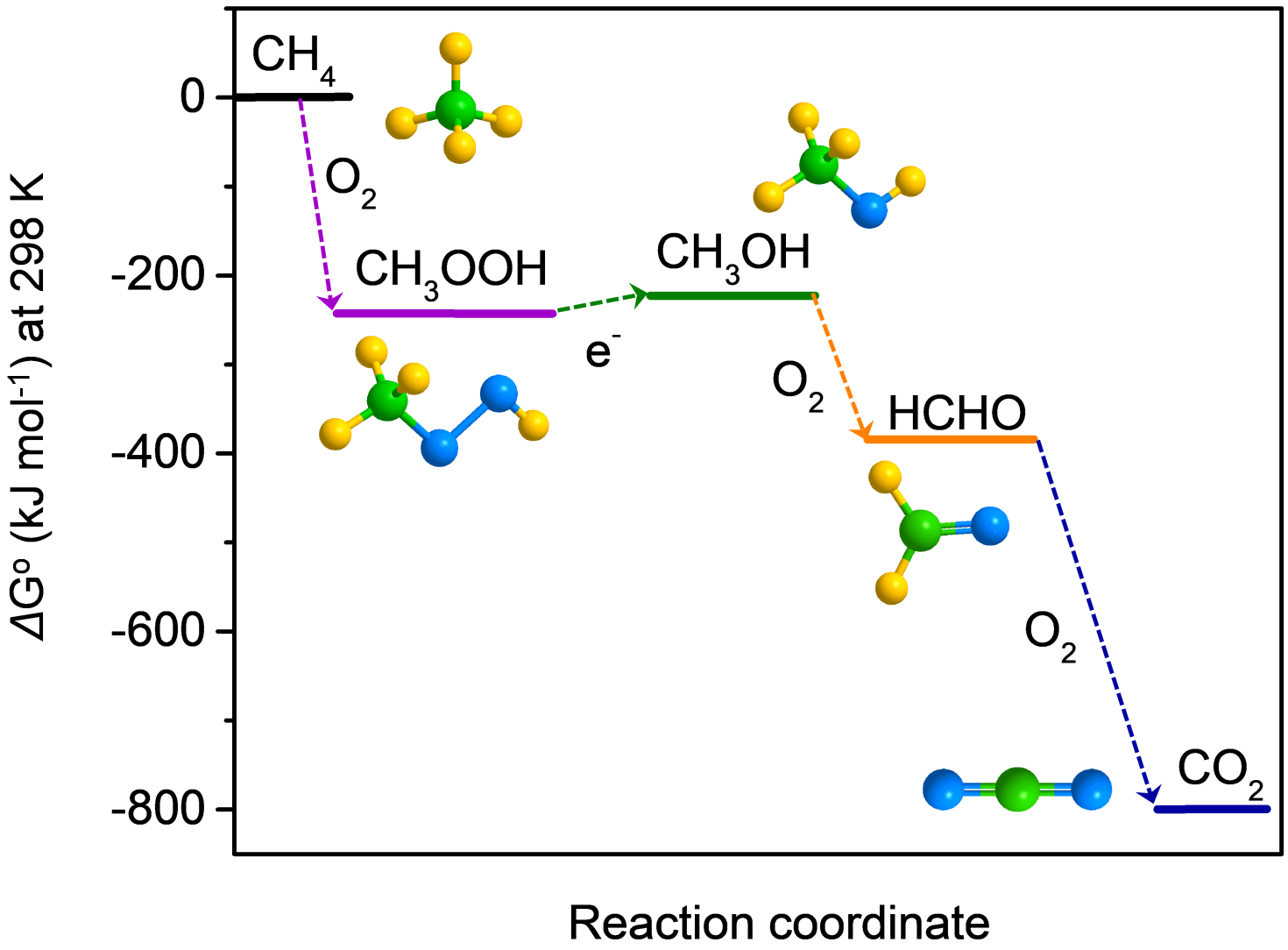

Figure 1

Gibbs free energy corresponding to formation of CH3OOH, CH3OH, HCHO and CO2 from CH4 oxidation at 298 K. Thermodynamic calculation highlights that selective oxidation of CH4 to CH3OH or HCHO is quite challenging since the requirement of sufficient reactant conversion and self-peroxidation prevention.

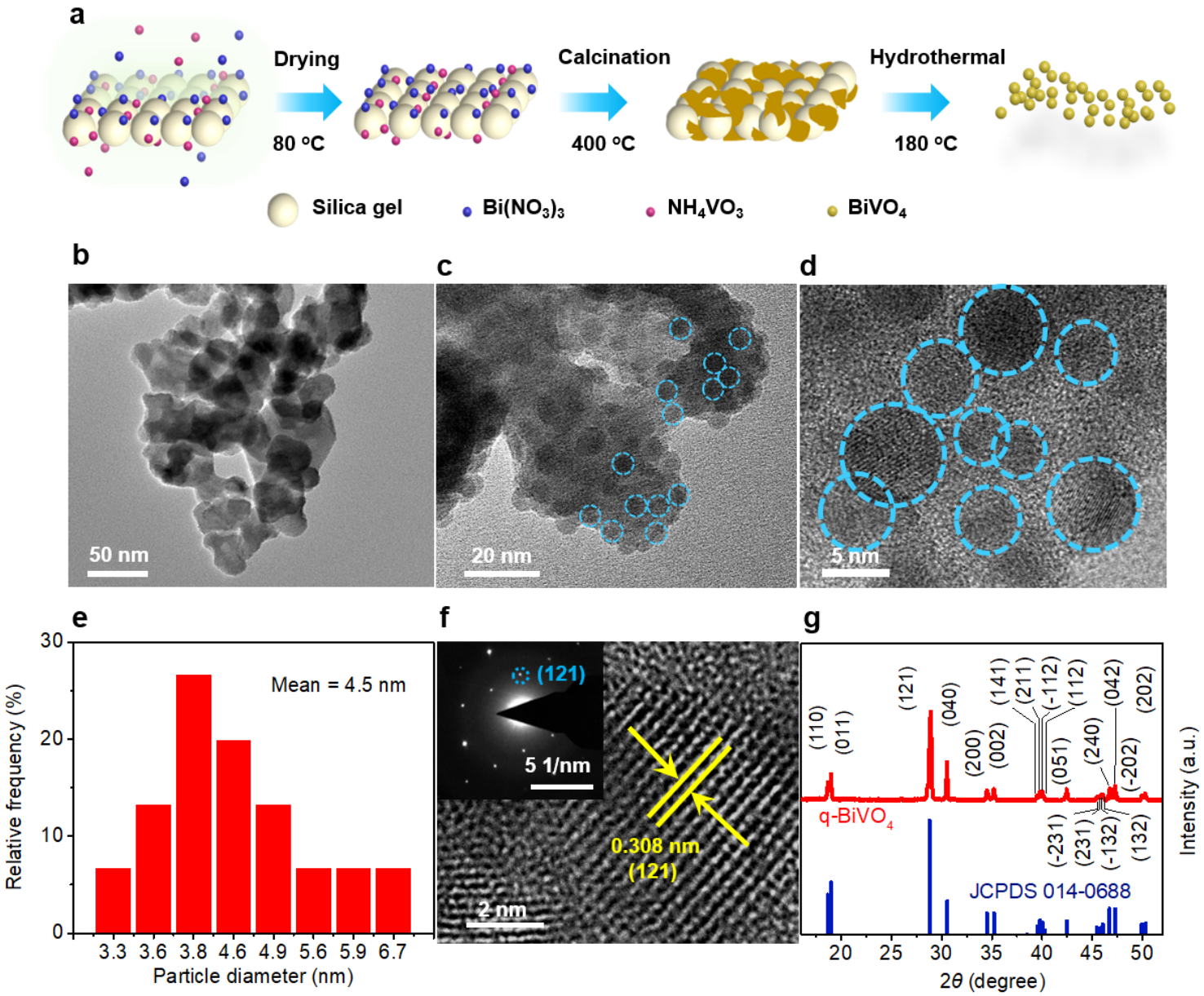

Figure 2

Synthesis and characterization of q-BiVO4. (a) Scheme for synthetic route of q-BiVO4. (b, c, d) Representative TEM images and (e) particle size distribution of q-BiVO4. (f) HRTEM and SAED images of q-BiVO4. The spacing of lattice fringe is 0.308 nm, corresponding to (121) facet. (g) XRD patterns of q-BiVO4. The crystal structure of q-BiVO4 is in perfect agreement with standard card (JCPDS 014-0688) of monoclinic scheelite structure.

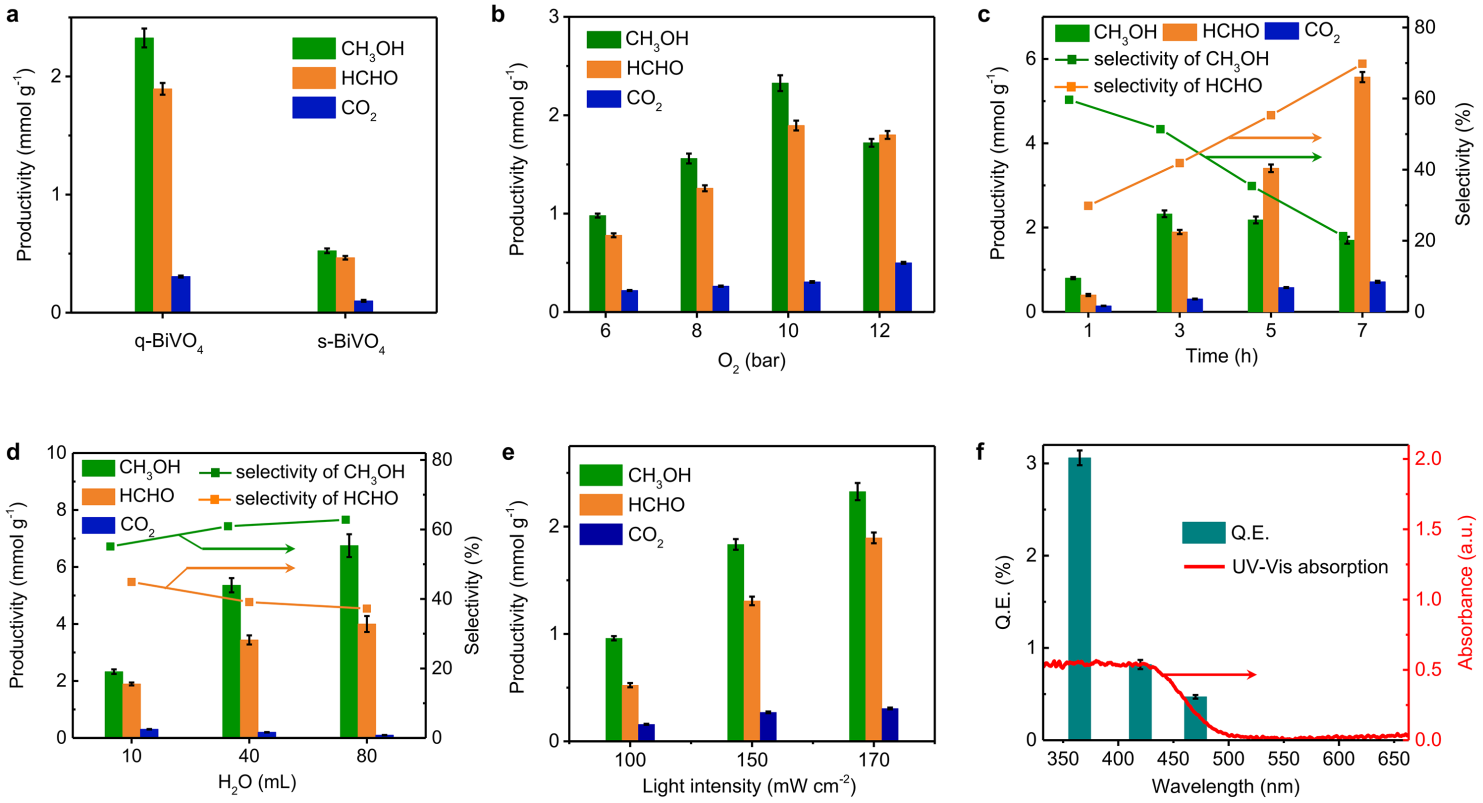

Figure 3

Photocatalytic oxidations of CH4 at different conditions. Productivity of oxygenates from CH4 oxidation with (a) q-BiVO4 and s-BiVO4 as photocatalysts as well as (b) under different O2 pressure. Yield of oxygenates from CH4 oxidation with the selectivity of CH3OH and HCHO at (c) different reaction time and (d) different H2O amount. Reaction condition: 10 mg q-BiVO4, 10 bar O2, 10 bar CH4, 10 mL H2O, 3 h reaction time, Hg lamp with irradiation wavelength of 300-600 nm and light density of 170 mW cm-2. According to different experiment requirement, the reaction parameters are changed. (e) Productivity assessment of oxygenates at different light intensity under irradiation in the wavelength range from 300 to 600 nm. (f) Q.E. value from different wavelength with adjustable light intensity, 365 nm 27 mW cm-2, 420 nm 108 mW cm-2, 470 nm 100 mW cm-2, 535 nm 100 mW cm-2 and 630 nm 100 mW cm-2, along with the diffuse reflectance spectrum of q-BiVO4.

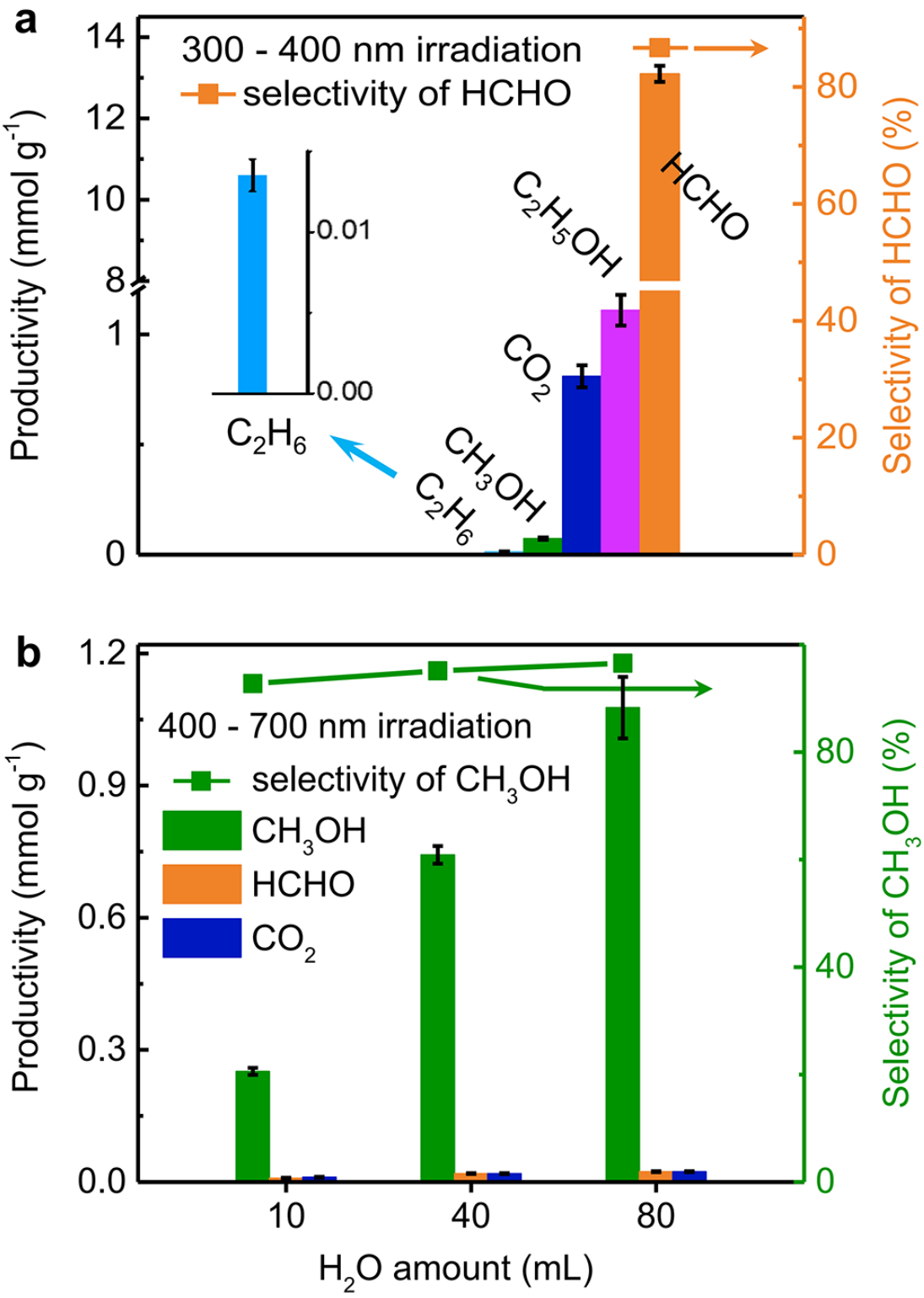

Figure 4

Selective oxidations of CH4. (a) Selective oxidation of CH4 to HCHO. (b) Selective oxidation of CH4 to CH3OH. Reaction condition: (a) 10 mg q-BiVO4, 10 bar O2, 10 bar CH4, 10 mL H2O, 7 h reaction time, Hg lamp with irradiation wavelength of 300-400 nm and light density of 170 mW cm-2. (b) 10 mg q-BiVO4, 10 bar O2, 10 bar CH4, 10-80 mL H2O, 3 h reaction time, Xenon lamp with irradiation wavelength of 400-780 nm and light intensity 170 mW cm-2.

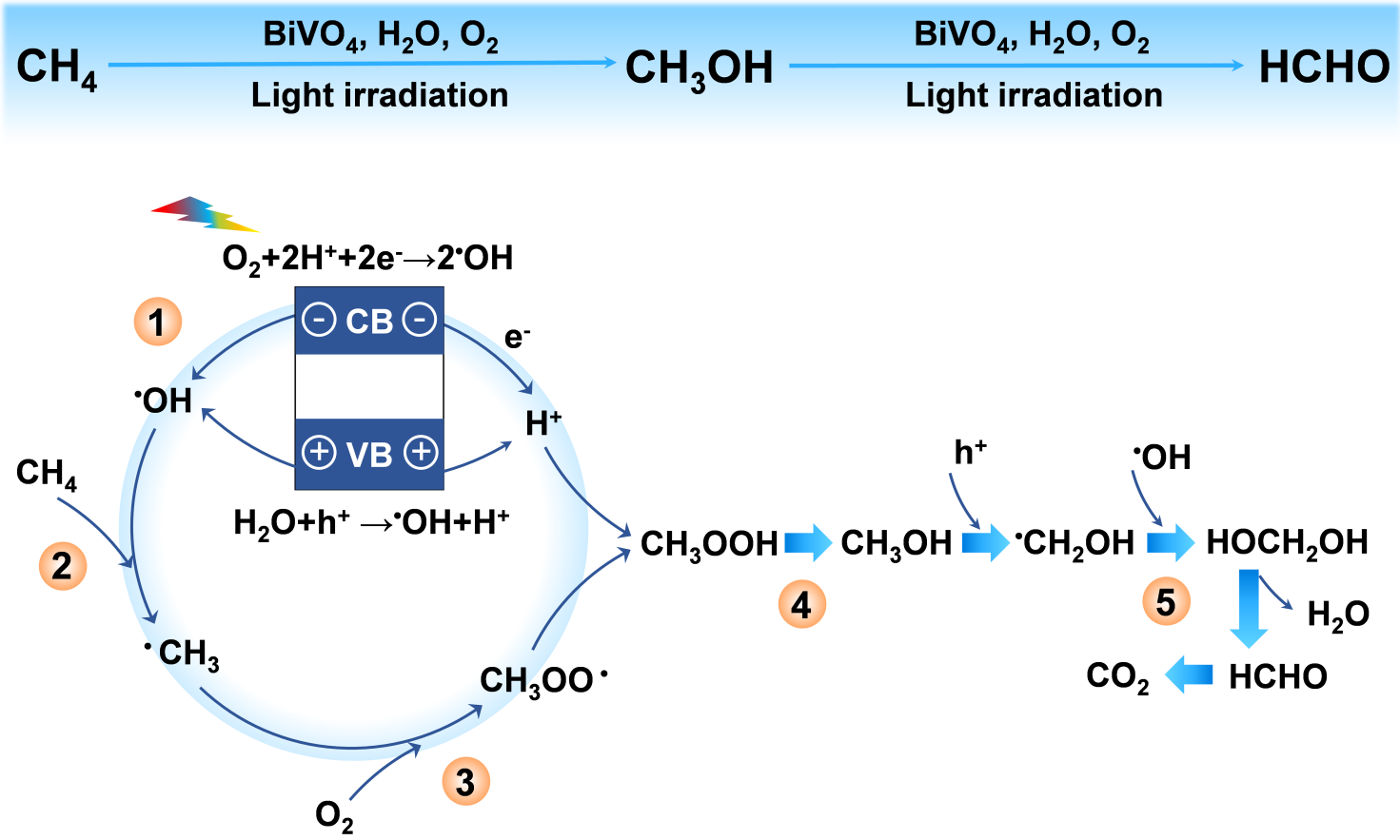

Figure 5

Proposed reaction mechanism for photocatalytic CH4 oxidation by q-BiVO4 in presences of H2O and O2.

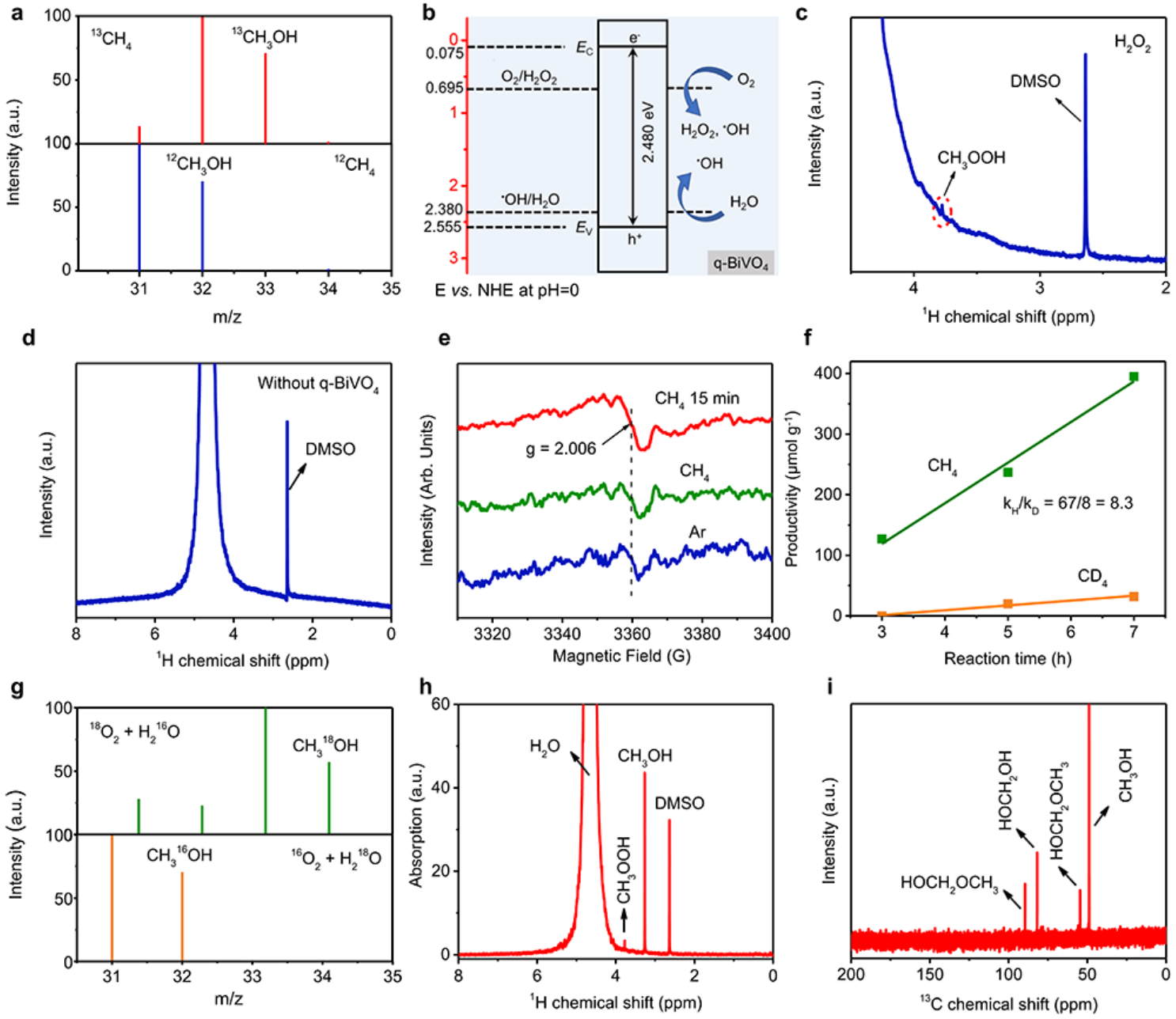

Figure 6

Stepwise analysis of reaction mechanism. (a) GC-MS spectra of CH3OH product carried out with 13CH4 and 12CH4, respectively. The m/z = 33 and 32 denote 13CH3OH and 12CH3OH, respectively. Other m/z peaks are attributed to the ionized fragments of CH3OH, such as 13CH3O+ (m/z = 32) and 12CH3O+ (m/z = 31). (b) Band energy diagram of q-BiVO4. (c) 1H NMR spectrum of the thermocatalytic product over q-BiVO4 at 60oC using H2O2 to provide •OH. (d) 1H NMR spectrum of the thermocatalytic product without q-BiVO4 at 60oC using H2O2 to provide •OH. (e) ESR spectra of q-BiVO4 subjected to Xenon irradiation in Ar or CH4 atmosphere. (f) Determining the rate-determining step based on KIE test. (g) GC-MS spectra of CH3OH formed by CH4 oxidation with 18O2 + H216O or 16O2 + H218O (mass = 32 and 34 stand for CH316OH and CH318OH, respectively). Other m/z peaks are attributed to the ionized fragments of CH3OH, such as CH318O+ (m/z = 33) and CH316O+ (m/z = 31). (h) 1H NMR spectrum obtained by 50

mg q-$BiVO_4$ dispersed in 0.5 mL water solvent for CH_4 conversion in order to increase the concentration of CH_3OOH. (i) 13C NMR spectrum of CH_3OH oxidation products through a similar photocatalytic system with Ar replacing CH_4.

Supplementary Files

This is a list of supplementary files associated with this preprint. Click to download.

- RevisedSupplementaryInformation.docx